Spectral Doppler Measurements with 2-D Sparse Arrays

(Article begins on next page)

18 May 2024

Spectral Doppler Measurements
with 2-D Sparse Arrays

Paolo Mattesini, Alessandro Ramalli, Lorena Petrusca, Olivier Basset, Hervé Liebgott,
and Piero Tortoli

Abstract—**Two-dimensional (2-D) sparse arrays, in which a few hundreds of elements are distributed on the probe surface according to an optimization procedure, represent an alternative to full 2-D arrays, including thousands of elements usually organized in a grid. Sparse arrays have already been used in B-mode imaging tests, but their application to Doppler investigations has not been reported yet. Since the sparsity of the elements influences the acoustic field, a corresponding influence on the mean frequency, bandwidth and signal to noise ratio of the Doppler spectra is expected.**

This paper aims to assess, by simulations and experiments, to what extent the use of a sparse rather than a full gridded 2-D array has an impact on spectral Doppler measurements. Parabolic flows were investigated by a 3 MHz, 1024-element gridded array and by a sparse array; the latter was obtained by properly selecting a sub-group of 256 elements from the full array. Simulations show that the mean Doppler frequency does not change between the sparse and the full array while there are significant differences on the bandwidth (average reduction of 17.2% for the sparse array, due to the different apertures of the two probes) and on the signal power (22 dB, due to the different number of active elements). These results are confirmed by flow phantom experiments, which also highlight that the most critical difference between sparse and full gridded array in Doppler measurements is in terms of signal-to-noise ratio (-16.8 dB).

Index Terms—**2-D arrays, 3-D imaging, sparse arrays, spectral Doppler measurements.**

I. INTRODUCTION

SPECTRAL Doppler analysis [1] still represents the reference ultrasound (US) investigation modality for quantitative blood velocity measurements [2]. It is widely used in cardiovascular imaging [3], e.g. for the assessment of artery stenosis or mitral valve regurgitation, as well as in obstetrics [4].

Recent advances in three-dimensional (3-D) US imaging [5] allow, in principle, extending Doppler analysis, so far limited within a planar region, to any point contained within a volume. This would be particularly useful, for example in carotid artery investigation, to contribute to the correct reconstruction of 3-D morphology of plaques that cannot be suitably described by standard B-Mode imaging [6]–[8].

Research efforts have been dedicated, in particular, to the development of novel 3-D vector flow imaging methods [9]–[13], but their experimental implementation is still limited. 3-D Doppler US is in fact typically based on 2-D array probes having many elements (up to thousands) that are usually organized in a grid. Such elements can be controlled by application of specific integrated circuits (ASICs) in high-end US machines [14], [15] or by using row-column addressed probes [16], [17]. An alternative, quite attractive in terms of cost and flexibility, is represented by 2-D sparse arrays [18]–[21]. In this case, a limited number of elements is distributed on the probe surface according to specific geometries, designed to optimize the acoustic beam both in transmission and reception (TX/RX) [22], [23]. Sparse arrays are attractive in terms of cost (as they do not need expensive ASICs, nor involve connectivity problems), and flexibility (since the elements can be individually controlled by the companion scanner to produce beams with different shapes and steering angles). Although sparse arrays have already been used in imaging tests [24], [25], their application to Doppler investigations has not been reported in the literature yet. Since the sparsity of the elements influences the acoustic field, a corresponding influence on the mean frequency, bandwidth and/or signal to noise ratio (SNR) of the Doppler spectra is expected.

The aim of this work is to experimentally assess to what extent the use of sparse rather than full (gridded) 2-D array impacts on spectral Doppler measurements. This topic was first discussed in the paper presented at IUS 2018 [26], which shows the preliminary results obtained with a rotating disk containing silicon particles in agar gel. This represents an almost ideal phantom, since all scatterers intercepted along a scan line produce the same Doppler spectrum, no clutter is involved, and attenuation is negligible. In this paper, Field II simulations [27], [28] are introduced, in which a parabolic flow is investigated by
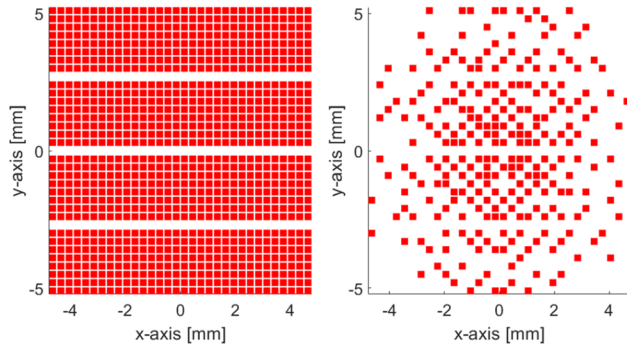
Fig. 1. Active elements distributions used in simulations and experiments: full gridded (ref1024: left) and sparse (opti256: right) arrays.

a full (1024-element) gridded array and a sparse array obtained by properly selecting a sub-group of 256 elements. Furthermore, exhaustive experimental tests are presented, conducted by using a more realistic phantom, in which a blood mimicking fluid flows in a tube surrounded by a tissue-mimicking material.

The paper is organized as follows: the section "Methods" describes the simulations, the equipment used for acquisitions, the experimental set-up, and the processing chain. The section "Results" reports the quantitative comparison of the performance obtained by a 1024-element, fully populated matrix probe and an optimized sparse probe with 256 elements. The results are then discussed in section IV, which aims at highlighting the most significant differences between the two cases.

II. METHODS

A. 2-D array probe

Simulations and experiments have been based on a 1024-element array probe with 3 MHz center frequency (Vermon, Tours, France). The element size is 249 μm and the pitch is 300 μm in both x and y directions, but 3 strips of elements are missing (see Fig.1). A sparse array configuration was derived from this probe by the optimum selection of 256 elements based on the simulated annealing approach [22]. As detailed in [29], the elements selection was optimized by controlling the pressure field behavior obtained at multiple depths.

The layout of the reference full gridded array (ref1024) and that of the sparse array (opti256) are shown in Fig. 1.

B. Simulations

The simulations set-up was maintained as much as possible close to the experimental set-up described in the next subsection.

Steady flow in a wall-less cylindrical pipe with a diameter (∅) of 5 mm and a length of 24 mm was simulated. Fully developed speckle was obtained by setting the density of the point scatterers to 8 scatterers/mm^3, which corresponds to at least 12 scatterers per resolution cell; in this paper, the smallest resolution cell was estimated to be 1.5 mm^3 for ref1024. The scatterers were moved with parabolic profile in steady laminar flow with peak velocity V_p = 40 cm/s. The vessel axis was set

parallel to the probe x-axis (see Fig. 2), at a depth z_a = 22.5 mm. The flow was simulated for a time interval ΔT = 1.82 s at a pulse repetition frequency PRF = 2250 Hz.

The acoustic beams associated to the 2-D probe used in the ref1024 and opti256 configurations were simulated with Field II. The TX beams were focused on the vessel axis by using 5-cycle sinusoidal bursts at 3 MHz. In reception, dynamic delay-and-sum beamforming without apodization was applied. Three steering angles were tested: 0°, 8° and 16° for each of two orthogonal planes (xz and yz). When steering over the yz plane, the probe was rotated by 90° to set the vessel axis parallel to the probe y-axis.

C. Experiments

The operations of four Vantage 256 scanners (Verasonics, Kirkland, USA) were synchronized to realize a 1024-channel system [30]. The channels were individually connected to the elements of ref1024 by means of 8 connectors. The scanners could be configured to use either all available elements of ref1024 or the 256 elements selected for opti256.

Unless otherwise stated, the TX signals were 5-cycle square bursts at 3 MHz frequency and 30V peak amplitude. The focal distance was always set coincident with the center of the investigated vessel. In reception, dynamic focusing without dynamic apodization was implemented. For each TX setting, raw echo-data were acquired for a time interval ΔT = 0.89 s at PRF = 2250 Hz, thus maximizing the use of the available memory onboard the scanners.

Acquisitions were based on the Doppler 403 Flow Phantom produced by Gammex (Middleton, WI, USA). This is a self-contained flow phantom including a 5-mm diameter (∅) vessel, surrounded by a tissue mimicking material (attenuation: 0.5 dB/cm/MHz), in which a blood mimicking fluid (Gammex patented Multi-Frequency HE [High Equivalency] Gel^{TM}) was forced to flow at 4 ml/s steady rate or in pulsatile conditions. The probe was placed on the phantom surface, parallel to the vessel, whose axis was at z_a = 22.5 mm, like in simulations. Three steering angles (θ = 0°, 8°, 16°) were tested in both the xz and yz planes (Fig. 2). As in simulations, when the TX beam was steered on the yz plane, the probe was rotated by 90°, so that such beam suitably intercepted the vessel axis. In all cases, efforts were done to maintain the same set-up conditions for consecutive measurements using the ref1024 and opti256 configurations. Since the main goal of the experiments was comparing the spectra obtained with the two probe lay-outs,
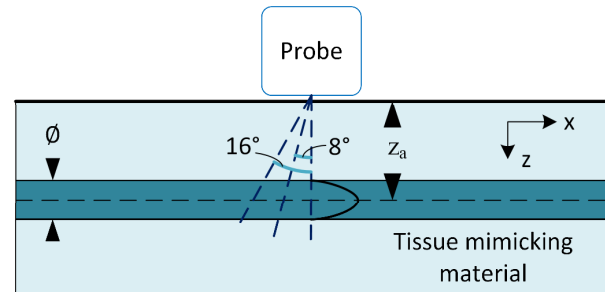

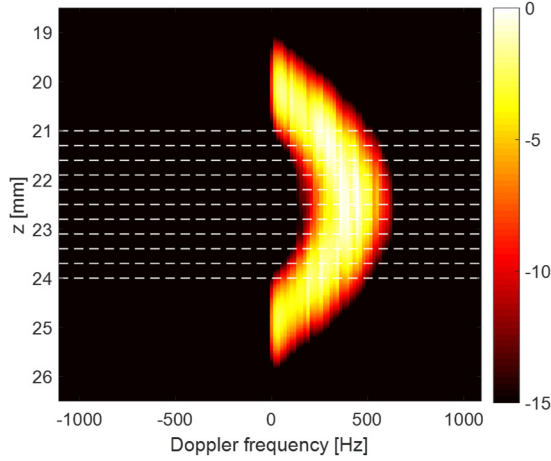Fig. 2. Schematic of the experimental and simulations set-up.

2

Fig. 3. Example of multi-gate spectral profile obtained in simulation with ref1024 producing a beam steered by 16° on the xz plane. For each depth, the spectral amplitudes are coded according to the color bar on the right. Dotted lines indicate the depths considered in the estimate of spectral parameters.
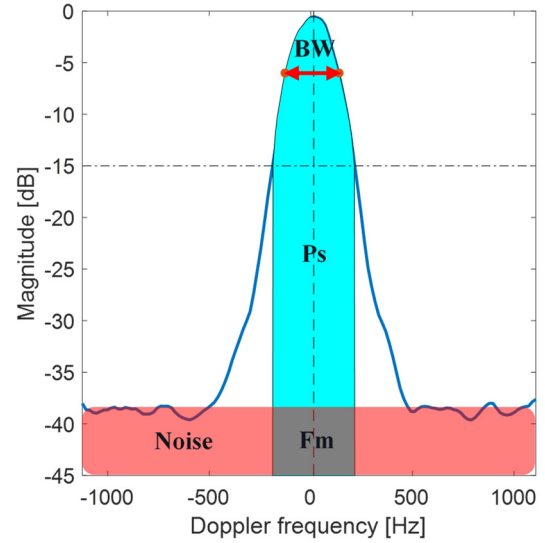

Fig. 4   Sample experimental Doppler spectrum obtained when all 1024 elements were used to transmit an unsteered beam. The figure shows how the spectral parameters (Fm, BW, Ps and noise) were evaluated.

possible slight misalignments between the vessel axis and the probe symmetry axis were disregarded.

D. Processing

Both simulated and experimental RF echo data received by all active elements were off-line beamformed, demodulated and low-pass filtered through MATLAB. The quadrature "slow-time" complex samples collected for each depth (i.e., the so-called Doppler signals), were gated with overlapping 128-point blocks, each weighted with a Blackman-Harris window, and then converted to the frequency domain by a 128-point FFT [31]. All the spectra computed for each depth, were finally averaged, except for the acquisitions in pulsatile flow conditions.

Fig. 3 shows an example of averaged multi-gate spectral profile [32], [33] obtained in simulation, when the beam produced by ref1024 was steered by 16° on the xz plane. In this profile, the power spectral Doppler densities detected at depths between 19 and 26 mm are coded according to the color bar shown on the right [32]. The dashed lines indicate the 11 specific depths (here spaced ≈ 0.3 mm apart) from which the averaged spectra were extracted to evaluate the performance, as detailed in the next paragraph. These depths have been chosen to be in the central zone of the vessel where flow velocities are clearly different from zero.

E. Performance metrics

For each Doppler spectrum extracted from simulations and experiments, the mean frequency (Fm), the -6dB bandwidth (BW) and the signal power (Ps) were estimated (see Fig. 4). The signal-to-noise ratio (SNR) was assessed for experimental data only. Ps was evaluated as the integral of the power spectral densities above a heuristic threshold (set at -15 dB) higher than the detected system noise. Based on the experimental results, the noise could be assumed as white; hence, its power spectral densities could be estimated over the frequency range [–PRF/2

–PRF/4] that, in all experiments, did not contain significant signal contributions.

The ref1024 and opti256 spectral values estimated for each steering angle were compared by calculating their (relative) differences as:

$$\Delta Fm = \frac{Fm_{opti256} - Fm_{ref1024}}{Fm_{ref1024}} \qquad (1)$$

$$\Delta BW = \frac{BW_{opti256} - BW_{ref1024}}{BW_{ref1024}} \qquad (2)$$

$$\Delta Ps = \frac{Ps_{opti256}}{Ps_{ref1024}} \qquad (3)$$

$$\Delta SNR = \frac{SNR_{opti256}}{SNR_{ref1024}} \qquad (4)$$

For each simulation/experiment, the above parameters were expressed by the average and the standard deviation (SD) of the spectral values measured at 11 different depths, as detailed in section II-D and Fig. 3.

III. RESULTS

A. Simulations

Fig. 5 shows six examples of spectra obtained in simulations for different steering angles. All such spectra are related to a sample volume overlapped to the vessel axis. The bottom panels, in particular, show that when the beam was steered on the yz plane, sidelobes lower than 25 dB (not visible when steering on the xz plane) appear for both configurations.

The figure highlights that the peak position is almost the same with both layouts and that the spectra of ref1024 feature wider bandwidths. These evaluations are confirmed by the simulation results reported in Table I. On average: for Fm, the

3

difference between ref1024 and opti256 was 0.5%, BW was reduced by 17.2% and Ps was reduced by 22 dB in opti256 compared to ref1024.

B. Flow phantom experiments

Fig. 6 shows two examples of multi-gate spectral Doppler profiles obtained from flow phantom experiments using ref1024 and opti256 probe configurations, respectively. In both cases, parabolic flow profiles are clearly detected over quite similar ranges of Doppler frequencies.

Fig. 7 shows three sample spectra corresponding to the sample volume intercepting the highest velocity when the flow was insonified at different steering angles (0°, 8°, 16°). It may be observed that the shape and the frequency of maximum spectral amplitude (approximately corresponding to the mean frequency) remain similar for both probe configurations, while the signal and noise levels are considerably different. Noise spectral density is about 6 dB higher for ref1024, consistent with the 4-fold larger number of elements/channels that contribute to the receiver wideband noise. On the other hand, the signal power is considerably lower for opti256 (-20/-28 dB), due to the 4-fold lower transmitted pressure and number of receiver channels.

This behaviour is confirmed by the measurements summarized in Table II: an average difference of 24 dB between the ref1024 and opti256 signal power detected in the different steering conditions, with a pronounced worsening at the highest steering angle. The corresponding SNR difference between

TABLE I
SIMULATION PERFORMANCE METRICS

Steering [°]		opti256 vs ref1024		
xz	yz	ΔFm ± SD [%]	ΔBW ± SD [%]	ΔPs ± SD [dB]
0	0	_a	-23.5±6.3	-22±0.08
8	0	-0.8±1.7	-19.5±5.4	-22±0.11
16	0	-0.7±1.2	-16±7.9	-21.9±0.04
0	0	_a	-15.2±6.5	-22.2±0.48
0	8	1.8±1.9	-15.2±3.1	-22±0.25
0	16	1.5±1.8	-13.5±5.2	-21.9±0.23
TOT:		0.5±1.6	-17.2±5.7	-22±0.20

a. ΔFm not evaluated because the nominal Doppler shift value is here zero

ref1024 and opti256 is, on average, 16.8 dB.

Fig. 8 shows the spectra obtained when the TX beam was steered by 8° on xz (top image) and by 8° on yz planes (bottom image). The spectra were obtained by using, for opti256, a double TX amplitude (30V) compared to that used for ref1024 (15V). It can be observed that the difference between spectral noise densities, depending only on the number of RX channels, is the same as in Fig. 7 (about 6 dB), while the difference in signal power is more limited (18 dB). Accordingly, the SNR for opti256 results only 11.8 dB worse than for ref1024.

IV. DISCUSSION

The main purpose of this paper was to evaluate to what extent a sparse element configuration, optimized to produce ultrasound focused beams, may influence the results of spectral
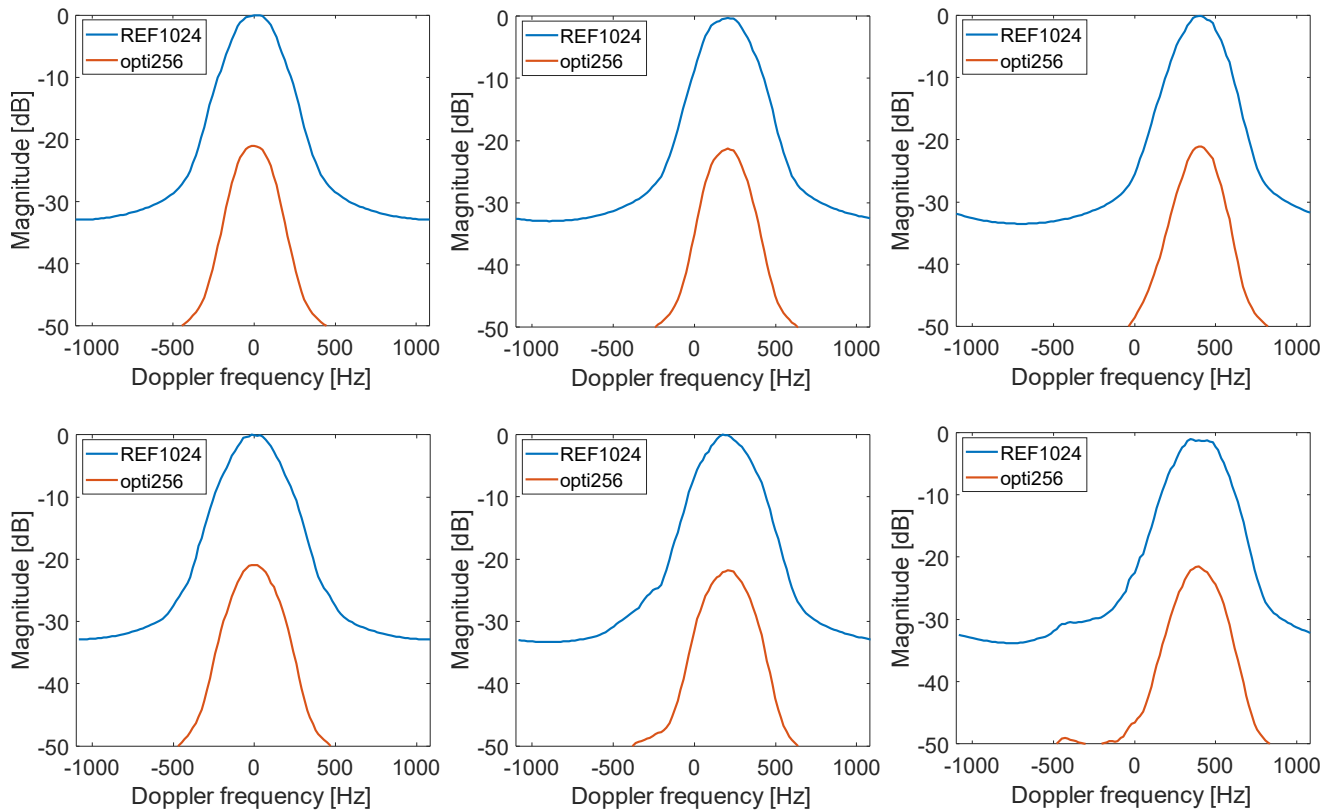

Fig. 5.   Examples of simulated Doppler spectra obtained for the two probe configurations at 0° (left), 8° (center) and 16° (right) steering in the xz plane (top) and in yz plane (bottom).
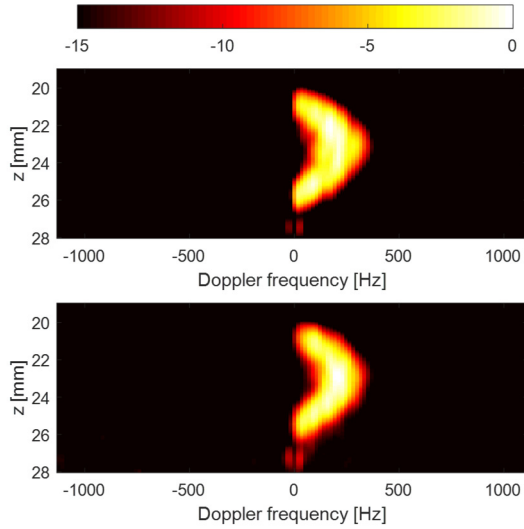
4

Fig. 6. Examples of multi-gate spectral Doppler obtained with ref1024 (top) and opti256 (bottom) with 16° of steering on xz plane on the flow phantom. Each profile is normalized to the respective peak spectral density.

Doppler investigations.

For both simulations and experiments, we chose the opti256 configuration as representative example of sparse array. Such configuration was in fact demonstrated capable of providing images of fair quality [24], which were also positively compared to the images produced by a "fully random" sparse array probe, rand256 (i.e., a probe whose random elements distribution was obtained choosing the best random configuration using the same number of iterations used to find opti256). The rand256 probe was not considered here because preliminary experiments related to a rotating disk phantom [26], have confirmed that the spectral Doppler results provided by rand256 are equivalent to (although slightly worse than) the results obtained with opti256.

Simulation results clearly show that, for all tested steering conditions, the Doppler spectrum shape and the mean frequency, F_m, are virtually unchanged when the sparse, rather than the fully populated array is used. For F_m, the average difference was only 0.5%. On the other hand, as shown in Fig. 5 and confirmed by Table I, the Doppler bandwidths detected by

TABLE II
EXPERIMENTAL PERFORMANCE METRICS

Steering [°]		opti256 vs ref1024			
xz	yz	ΔFm ± SD [%]	ΔBW ± SD [%]	ΔPs ± SD [dB]	ΔSNR ± SD [dB]
0	0	-^{b}	-30.9±6.1	-24.8±0. 5	-17.6±0.6
8	0	5.5±7.2	-20.6±5.8	-24.9±0.2	-17.8±0.3
16	0	-1.4±6.2	-8.2±12.5	-27.6±0.6	-20.9±0.6
0	0	-^{b}	-20.7±4.8	-25.3±0.2	-17.8±0.4
0	8	2.4±7.1	-19.3±9.8	-21.3±0.5	-14.3±0.5
0	16	2.1±11.5	-9.9±8.6	-19.8±0.2	-12.5±0.4
TOT:		2.2±8	-18.3±7.9	-24±0.4	-16.8±0.5

b. ΔFm not evaluated because the nominal Doppler shift value is here zero

the sparse array probe are significantly narrower. This result looks consistent with the different equivalent apertures of the two probes. In fact, as reported in [1], [34]–[37], due to transit-time broadening, the resulting BW is proportional to the equivalent aperture, A, of the probe. Approximating this as twice the average distance between the position of the elements and the center of the probe, A resulted in 6 and 7.8 mm for opti256 and ref1024, respectively. The ratio between the two apertures is thus 77%. If we consider, in particular, the measurements performed at a beam-to-flow angle of 0°, in which the bandwidth is proportional to the aperture and to the highest intercepted velocity (but is not influenced by the possible presence of lower velocities within the sample volume [28]) the average bandwidth reduction for opti256 results 17.2%, in fair agreement with the 77% ratio between the two equivalent probe apertures. However, since the velocity was estimated from the spectral mean frequency, the reduction in spectral bandwidth does not influence the velocity uncertainty, while it should be taken into consideration in possible velocity measurements based on spectral peak frequency [38]. Due to the asymmetrical lay-out of the used probe (which, in particular, includes three missing lines on the y-direction) the US beams resulted not symmetrical around the probe axis: according to simulations, for opti256, the -6dB beamwidths along the x- and y-axis were 1.75 mm and 1.47 mm, respectively; for ref1024 they were 1.31 and mm and 1.20 mm. For example, such different beamwidths involve different ΔBWs in the two 0°-0° cases reported in Table I and in Table II.

Simulations have also shown that when US beams are steered within the yz plane, low-level spectral sidelobes appear for both
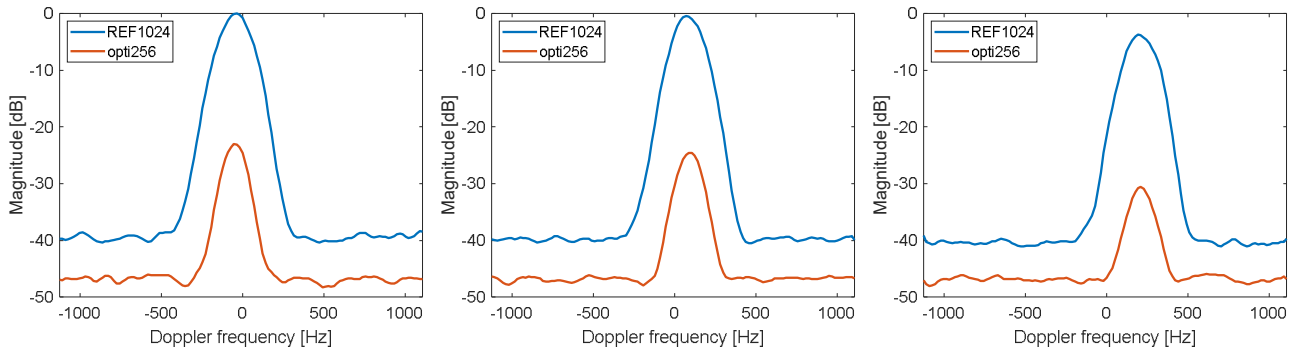

Fig. 7. Examples of experimental Doppler spectra obtained for the two probe configurations when the flow phantom was intercepted by US beams produced with 0° (left), 8° (center) and 16° (right) steering angles in the xz plane.
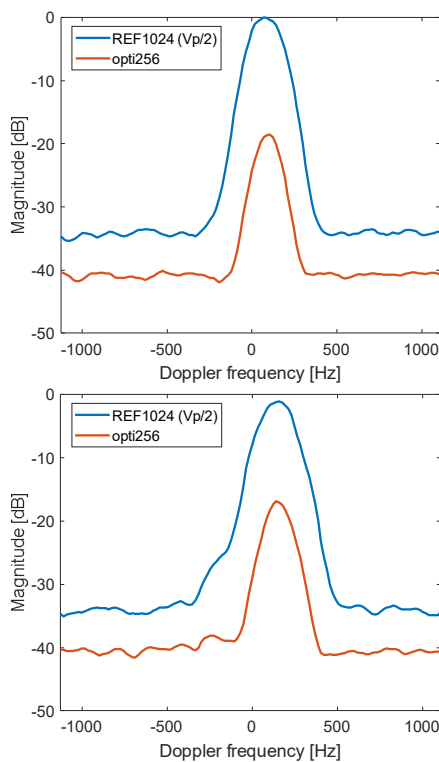
5

Fig. 8. Examples of Doppler spectra obtained on the horizontal vessel with 8° steering on xz plane (top) and on yz plane (bottom). The spectrum of ref1024 are acquired using a lower excitation voltage.

configurations (Fig. 5). In Fig.8, a small (<-20dB) sidelobe is visible for ref1024 but not for opti256, probably because it is hidden by noise. Considering that such sidelobes have not emerged when steering was within the xz plane, they can be attributed to the three missing rows of elements (see Fig. 1, left panel), which determine a local double-pitch along the y-axis.

The experimental measurements have confirmed the invariance of spectrum shape and mean frequency with the probe element distribution (Table II, Fig. 6-8). Moreover, spectrograms like those in Fig. 9 show that the Doppler spectra remain qualitatively similar also in non-steady flow conditions. The time-trends of the mean Doppler frequency (blue solid lines) were estimated for both the array configurations and compared by computing the Pearson product-moment correlation coefficient. This was $r = 0.856$, which represents a good statistical relationship, especially considering the noise level on the spectrograms and the limited signal power achieved with opti256.

The experimental set-up was not always able to guarantee an accurate alignment of the probe axis with the vessel. For example, the slight negative Doppler shift in the first panel of Fig. 7 (the case without steering) was due to setting a Doppler angle not exactly at 90° as desired. However, since the main goal was comparing the spectra obtained with ref1024 and opti256, we took care that the same set-up conditions were maintained for consecutive measurements based on the two array configurations.

More relevant are the flexibility limitations of the experimental set-up, which did not permit accurately testing

conditions in which the vessel axis was either at different depths or intercepted by beams steered along planes other than xz and yz. However, the multi-gate spectral Doppler approach provides Doppler spectra at different depths. Although these spectra are not shown here, the results in Table I and II, reporting average and standard deviation values at different depths, confirm the main findings of this paper. Furthermore, steering conditions other than those reported in this paper could be simulated, and the obtained Doppler spectra resulted very similar to those shown in Fig. 5. Also, additional simulations were performed with another sparse array including 128 elements (opti128: see [29]) and they confirmed the invariance of Fm as well as the BW reduction due to a reduced equivalent aperture of the sparse array. Obviously, the Ps also was reduced since the halved of the elements number.

The major differences between the experimental results obtained with 256 or 1024 elements are related to the signal and the noise power. Concerning the signal power, when the same TX voltages are used, 24 dB difference between ref1024 and opti256 distributions are expected. In fact, the 4-fold lower number of TX-RX elements involves an average pressure reduction of 12 dB and, assuming full coherence between all RX channel signals, a further reduction of 12 dB in the receiver. On the other hand, the number of channels that contribute to the
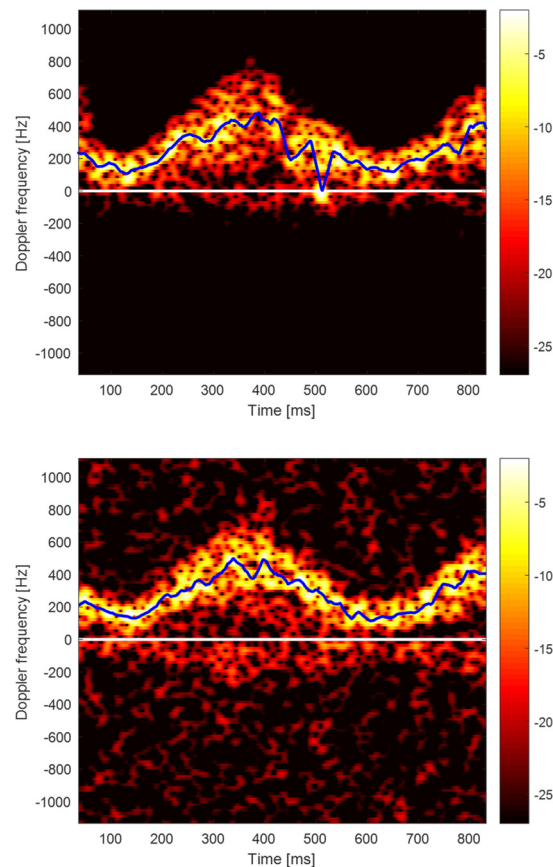

Fig. 9. Examples of spectrograms obtained with ref1024 (top) and opti256 (bottom) with 16° of steering on yz plane on the flow phantom (the dynamic range was 25dB in both panels while the gain was adjusted to highlight the different SNRs).

6

received noise is 4-times larger for ref1024. This involves that the total noise at the beamformer output should be 6 dB higher than in the 256-element cases. In total, when 256 elements are used, instead of the 1024 available in the full probe, we expect, on average, about 24-6=18 dB SNR degradation. The experimental results are consistent with such prediction, since using ref1024, the average SNR improvement was 16.8 dB with 0.5 standard deviation.

The SNR loss may severely limit the in vivo maximum penetration depth, excluding, for example, the Doppler investigation of deep vessels. This limitation could be partially overcome by exciting the sparse array probe elements with higher TX voltages, to produce the same focal pressure (i.e., same Mechanical Index) as the full array, provided possible effects on the Thermal Index are taken under control. Also, coded imaging techniques, which have been already shown capable of increasing by up to 12dB the SNR in Doppler investigation [39], could be exploited.

It is worth mentioning that the comparison among the different arrays was done without applying any apodization both in transmission and in reception to maximize the sensitivity and SNR. In a real-case scenario, apodization would be applied to ref1024 to reduce side-lobes, thus narrowing the effective aperture and hence reducing the Doppler bandwidth. On the other hand, the density of the active elements of opti256 increases towards the center, i.e. a sort of density tapering resulted from the constraints imposed on the beam pattern during the optimization process. Hence, the beam shape was already optimized and any further apodization, not only would further limit its sensitivity but would also deteriorate its performance.

Future work will be addressed to solve the current limitations of the experimental set-up, so that investigation of further angle and focal depth combinations will be possible, and to provide, in particular, a reliable real-time display, which will be essential for preliminary *in-vivo* tests.

V. CONCLUSION

In this study, we have shown that the use of sparse arrays rather than full gridded ones in spectral Doppler measurements does not affect the mean Doppler frequency nor introduces spectrum distortions, but it may impact on the Doppler bandwidth. In fact, the bandwidth depends on the probe equivalent aperture, which may be significantly different (as in the case reported in this paper) in the sparse and in the reference full array. Furthermore, the major limitation of sparse arrays is the reduced penetration depth that, for *in-vivo* applicability, might require the implementation of advanced transmission and signal processing techniques to recover the SNR.

In conclusion, taken the appropriate countermeasures to limit the impact of their reduced sensitivity, sparse arrays can be suitably employed for Doppler measurements. Of course, as for 1-D arrays, the layout and electro-acoustic characteristics should be optimized to adapt sparse arrays to every specific application.

REFERENCES

[1] Ph. D. Evans D. H. and W. N. McDicken, *Doppler ultrasound: physics, instrumentation, and signal processing*, 2nd ed. Chichester ; New York : J. Wiley, 2000.

[2] Y. Karabiyik, I. K. Ekroll, S. H. Eik-Nes, and L. Lovstakken, "Quantitative Doppler Analysis Using Conventional Color Flow Imaging Acquisitions," *IEEE Transactions on Ultrasonics, Ferroelectrics, and Frequency Control*, vol. 65, no. 5, pp. 697–708, May 2018.

[3] I. K. Ekroll, T. Dahl, H. Torp, and L. Løvstakken, "Combined vector velocity and spectral Doppler imaging for improved imaging of complex blood flow in the carotid arteries," *Ultrasound Med Biol*, vol. 40, no. 7, pp. 1629–1640, Jul. 2014.

[4] G. Urban *et al.*, "State of the Art: Non-Invasive Ultrasound Assessment of the Uteroplacental Circulation," *Seminars in Perinatology*, vol. 31, no. 4, pp. 232–239, Aug. 2007.

[5] A. Fenster, D. B. Downey, and H. N. Cardinal, "Three-dimensional ultrasound imaging," *Phys. Med. Biol.*, vol. 46, no. 5, pp. R67–R99, Apr. 2001.

[6] G. A. Roth *et al.*, "Global, Regional, and National Burden of Cardiovascular Diseases for 10 Causes, 1990 to 2015," *J. Am. Coll. Cardiol.*, vol. 70, no. 1, pp. 1–25, Jul. 2017.

[7] M. Kozàkovà, C. Morizzo, F. Andreucetti, P. Palchetti, G. Parenti, and C. Palombo, "Quantification of extracranial carotid artery stenosis by ultrafast three-dimensional ultrasound," *Journal of the American Society of Echocardiography*, vol. 14, no. 12, pp. 1203–1211, Dec. 2001.

[8] B. López-Melgar *et al.*, "Accurate quantification of atherosclerotic plaque volume by 3D vascular ultrasound using the volumetric linear array method," *Atherosclerosis*, vol. 248, pp. 230–237, May 2016.

[9] J. A. Jensen, S. I. Nikolov, A. C. H. Yu, and D. Garcia, "Ultrasound Vector Flow Imaging—Part I: Sequential Systems," *IEEE Transactions on Ultrasonics, Ferroelectrics, and Frequency Control*, vol. 63, no. 11, pp. 1704–1721, Nov. 2016.

[10] J. Avdal, L. Løvstakken, H. Torp, and I. K. Ekroll, "Combined 2-D Vector Velocity Imaging and Tracking Doppler for Improved Vascular Blood Velocity Quantification," *IEEE Transactions on Ultrasonics, Ferroelectrics, and Frequency Control*, vol. 64, no. 12, pp. 1795–1804, Dec. 2017.

[11] S. Holbek *et al.*, "Ultrasonic 3-D Vector Flow Method for QuantitativeIn VivoPeak Velocity and Flow Rate Estimation," *IEEE Transactions on Ultrasonics, Ferroelectrics, and Frequency Control*, vol. 64, no. 3, pp. 544–554, Mar. 2017.

[12] M. S. Wigen *et al.*, "4-D Intracardiac Ultrasound Vector Flow Imaging–Feasibility and Comparison to Phase-Contrast MRI," *IEEE Transactions on Medical Imaging*, vol. 37, no. 12, pp. 2619–2629, Dec. 2018.

[13] S. Fiorentini, L. M. Saxhaug, T. G. Bjåstad, E. Holte, H. Torp, and J. Avdal, "Maximum Velocity Estimation in Coronary Arteries Using 3-D Tracking Doppler," *IEEE Transactions on Ultrasonics, Ferroelectrics, and Frequency Control*, vol. 65, no. 7, pp. 1102–1110, Jul. 2018.

[14] I. O. Wygant *et al.*, "An integrated circuit with transmit beamforming flip-chip bonded to a 2-D CMUT array for 3-D ultrasound imaging,"

IEEE Transactions on Ultrasonics, Ferroelectrics, and Frequency Control, vol. 56, no. 10, pp. 2145–2156, Oct. 2009.

[15] E. Kang *et al.*, "A Reconfigurable Ultrasound Transceiver ASIC with 24x40 Elements for 3-D Carotid Artery Imaging," *IEEE Journal of Solid-State Circuits*, vol. 53, no. 7, pp. 2065–2075, Jul. 2018.

[16] T. L. Christiansen, M. F. Rasmussen, J. P. Bagge, L. N. Moesner, J. A. Jensen, and E. V. Thomsen, "3-D imaging using row–column-addressed arrays with integrated apodization— part ii: transducer fabrication and experimental results," *IEEE Transactions on Ultrasonics, Ferroelectrics, and Frequency Control*, vol. 62, no. 5, pp. 959–971, May 2015.

[17] S. Holbek, T. L. Christiansen, M. B. Stuart, C. Beers, E. V. Thomsen, and J. A. Jensen, "3-D Vector Flow Estimation With Row–Column-Addressed Arrays," *IEEE Transactions on Ultrasonics, Ferroelectrics, and Frequency Control*, vol. 63, no. 11, pp. 1799–1814, Nov. 2016.

[18] A. Austeng and S. Holm, "Sparse 2-D arrays for 3-D phased array imaging - design methods," *IEEE Transactions on Ultrasonics, Ferroelectrics, and Frequency Control*, vol. 49, no. 8, pp. 1073–1086, Aug. 2002.

[19] A. Trucco, "Thinning and weighting of large planar arrays by simulated annealing," *IEEE Transactions on Ultrasonics, Ferroelectrics, and Frequency Control*, vol. 46, no. 2, pp. 347–355, Mar. 1999.

[20] B. Diarra, M. Robini, P. Tortoli, C. Cachard, and H. Liebgott, "Design of Optimal 2-D Nongrid Sparse Arrays for Medical Ultrasound," *IEEE Transactions on Biomedical Engineering*, vol. 60, no. 11, pp. 3093–3102, Nov. 2013.

[21] O. Martínez-Graullera, C. J. Martín, G. Godoy, and L. G. Ullate, "2D array design based on Fermat spiral for ultrasound imaging," *Ultrasonics*, vol. 50, no. 2, pp. 280–289, Feb. 2010.

[22] E. Roux, A. Ramalli, P. Tortoli, C. Cachard, M. Robini, and H. Liebgott, "2-D Ultrasound Sparse Arrays Multidepth Radiation Optimization Using Simulated Annealing and Spiral-Array Inspired Energy Functions," *IEEE Transactions on Ultrasonics, Ferroelectrics, and Frequency Control*, vol. 63, no. 12, pp. 2138–2149, Dec. 2016.

[23] A. Ramalli, E. Boni, A. S. Savoia, and P. Tortoli, "Density-tapered spiral arrays for ultrasound 3-D imaging," *IEEE Transactions on Ultrasonics, Ferroelectrics, and Frequency Control*, vol. 62, no. 8, pp. 1580–1588, Aug. 2015.

[24] E. Roux, F. Varray, L. Petrusca, C. Cachard, P. Tortoli, and H. Liebgott, "Experimental 3-D Ultrasound Imaging with 2-D Sparse Arrays using Focused and Diverging Waves," *Scientific Reports*, vol. 8, no. 1, p. 9108, Jun. 2018.

[25] A. Austeng and S. Holm, "Sparse 2-D arrays for 3-D phased array imaging - experimental validation," *IEEE Transactions on Ultrasonics, Ferroelectrics, and Frequency Control*, vol. 49, no. 8, pp. 1087–1093, Aug. 2002.

[26] P. Mattesini *et al.*, "Spectral Doppler Measurements with 2-D Sparse Arrays," in *2018 IEEE International Ultrasonics Symposium (IUS)*, 2018, pp. 1–4.

[27] J. A. Jensen, "FIELD: A Program for Simulating Ultrasound Systems," in *10th Nordicbaltic Conference on Biomedical Imaging, Vol. 4, Supplement 1, Part 1:351–353*, 1996, pp. 351–353.

[28] J. A. Jensen and N. B. Svendsen, "Calculation of pressure fields from arbitrarily shaped, apodized, and excited ultrasound transducers," *IEEE Transactions on Ultrasonics, Ferroelectrics, and Frequency Control*, vol. 39, no. 2, pp. 262–267, Mar. 1992.

[29] E. Roux, A. Ramalli, H. Liebgott, C. Cachard, M. C. Robini, and P. Tortoli, "Wideband 2-D Array Design Optimization With Fabrication Constraints for 3-D US Imaging," *IEEE Transactions on Ultrasonics, Ferroelectrics, and Frequency Control*, vol. 64, no. 1, pp. 108–125, Jan. 2017.

[30] L. Petrusca *et al.*, "Fast Volumetric Ultrasound B-Mode and Doppler Imaging with a New High-Channels Density Platform for Advanced 4D Cardiac Imaging/Therapy," *Applied Sciences*, vol. 8, no. 2, Feb. 2018.

[31] P. Tortoli, G. Guidi, P. Berti, F. Guidi, and D. Righi, "An FFT-based flow profiler for high-resolution in vivo investigations," *Ultrasound in Medicine & Biology*, vol. 23, no. 6, pp. 899–910, Jan. 1997.

[32] P. Tortoli, G. Bambi, F. Guidi, and R. Muchada, "Toward a better quantitative measurement of aortic flow," *Ultrasound in Medicine and Biology*, vol. 28, no. 2, pp. 249–257, Feb. 2002.

[33] P. Tortoli, F. Guidi, G. Guidi, and C. Atzeni, "Spectral velocity profiles for detailed ultrasound flow analysis," *IEEE Transactions on Ultrasonics, Ferroelectrics, and Frequency Control*, vol. 43, no. 4, pp. 654–659, Jul. 1996.

[34] V. L. Newhouse, E. S. Furgason, G. F. Johnson, and D. A. Wolf, "The Dependence of Ultrasound Doppler Bandwidth on Beam Geometry," *IEEE Transactions on Sonics and Ultrasonics*, vol. 27, no. 2, pp. 50–59, Mar. 1980.

[35] P. Tortoli, G. Guidi, and P. Pignoli, "Transverse Doppler spectral analysis for a correct interpretation of flow sonograms," *Ultrasound in Medicine and Biology*, vol. 19, no. 2, pp. 115–121, Jan. 1993.

[36] G. Guidi, C. Licciardello, and S. Falteri, "Intrinsic spectral broadening (ISB) in ultrasound Doppler as a combination of transit time and local geometrical broadening," *Ultrasound in Medicine and Biology*, vol. 26, no. 5, pp. 853–862, Jun. 2000.

[37] A. C. H. Yu, A. H. Steinman, and R. S. C. Cobbold, "Transit-time broadening in pulsed Doppler ultrasound: a generalized amplitude modulation model," *IEEE Transactions on Ultrasonics, Ferroelectrics, and Frequency Control*, vol. 53, no. 3, pp. 530–541, Mar. 2006.

[38] P. Tortoli, G. Guidi, and V. L. Newhouse, "Improved blood velocity estimation using the maximum Doppler frequency," *Ultrasound Med Biol*, vol. 21, no. 4, pp. 527–532, 1995.

[39] A. Ramalli, E. Boni, A. Dallai, F. Guidi, S. Ricci, and P. Tortoli, "Coded Spectral Doppler Imaging: From Simulation to Real-Time Processing," *IEEE Transactions on Ultrasonics, Ferroelectrics, and Frequency Control*, vol. 63, no. 11, pp. 1815–1824, Nov. 2016.